Equi-intensity distribution of optical reflectance in a fibrous turbid medium

Ali Shuaib and Gang Yao*

Department of Biological Engineering, University of Missouri, Columbia, Missouri 65211, USA

*Corresponding author: yaog@missouri.edu

Received 16 September 2009; revised 22 December 2009; accepted 14 January 2010; posted 15 January 2010 (Doc. ID 117241); published 3 February 2010

Light propagation in a fibrous anisotropic scattering medium is quite different from that in an isotropic medium. Both the anisotropic diffuse equation (ADE) and the continuous time random walk (CTRW) theory predict that the equi-intensity profiles of the surface reflectance have an elliptical shape in a fibrous turbid medium. In this study, we simulated the spatially resolved surface reflectance in a fibrous sample using a Monte Carlo model. A parametric equation was used to quantitatively characterize the geometric profiles of the reflectance patterns. The results indicated that the equi-intensity profiles of surface reflectance had elliptical shapes only when evaluated at distances far away from the incident point. The length ratio of the two orthogonal axes of the ellipse was not affected by the sample optical properties when the ratio of reduced scattering coefficients along the two axes is the same. But the relationship between the aforementioned two ratios was different from the predication of ADE theory. Only for fibers of small sizes did the fitted axes ratios approach the values predicted from the ADE theory.

OCIS codes: 290.1990, 290.1750.

1. Introduction

Optical methods have been widely used to study biological tissues. In many studies, the tissue sample can be assumed as isotropic, i.e., its optical properties are independent of photon incident directions. However, this is not true in some biological tissues such as muscle [1], skin [2], dentin [3], and white matter [4], where anisotropic fibrous or tubular structures are abundant. For example, Marquez *et al.* [1] found that optical properties of the chicken breast differed significantly when measured parallel or perpendicular to the muscle fiber orientation.

In order to describe light propagation in anisotropic tissue, the conventional isotropic diffuse equation can be modified [5,6] by replacing the scalar diffusion coefficient with a diffusion tensor. This anisotropic diffuse equation (ADE) model predicts that the equi-intensity profiles of the surface reflectance have elliptical shapes [7] in media with a predominant structural orientation (such as aligned fibers). The ellipse is elongated along the direction with a smaller reduced scattering coefficient. The ratio of the two primary axes of the ellipse is inversely proportional to the square root of the corresponding reduced scattering coefficients along the two axes.

In another approach, Dagdug *et al.* [8] extended the continuous time random walk (CTRW) theory to analyze light propagation in an anisotropic turbid medium by assigning different transition probabilities along different directions. In a fibrous sample, the model used a bias parameter B, defined as the ratio of the transition probability parallel with and perpendicular to the fiber's direction, to characterize the anisotropy. This model also predicts an elliptical pattern of the equi-intensity reflectance in fibrous tissues. The ratio of the two primary axes is proportional to the square root of the corresponding transitional probabilities.

The elliptical equi-intensity reflectance profile predicted from both ADE and CTRW models has been observed in several anisotropic tissue models [9–11]. Kienle *et al.* [12] showed that the equi-intensity

0003-6935/10/050838-07$15.00/0

profiles had different elliptical orientations at different evaluation distances in dentin. Nickell *et al.* [2] found that the elliptical reflectance profile in skin tissue was caused by the preferential orientation of the collagen fibers.

Kienle [13] studied spatial- and time-resolved diffuse transmission in fibrous anisotropic media and found the results obtained from ADE theory were very different from those obtained with Monte Carlo simulation. Kienle [13] proposed that Monte Carlo models based on light scattering by cylindrical structures [12] were more accurate for studying light propagation in fibrous scattering media. Schäfer and Kienle [14] proved that this approach had a good agreement with Maxwell theory based solutions when the volume cylinder density is small ($\rho < 10\%$). Several studies showed that the Monte Carlo simulation had good agreements with the experimental results obtained in porcine artery [12], dentin [15], and wood [16].

Although discrepancies were noticed when comparing the equi-intensity profiles of the diffuse transmittance obtained by ADE and Monte Carlo simulation [13], these differences have not been studied in detail. In this study, we applied Monte Carlo simulations to investigate the equi-intensity profiles of the diffuse reflectance in an anisotropic medium composed of a mixture of cylinders and spheres scatters. A parametric equation was used to describe quantitatively the reflectance images. The effects of the background optical properties and the cylinder size were investigated. We found that the Monte Carlo results approached the predictions of ADE theory when the cylinders have a smaller radius.

2. Methods

A. Simulation Model

The scattering medium model used in this study has been previously described by Kienle [12] to simulate anisotropic fibrous tissues. As shown in Fig. 1(a), the sample was a semi-infinite medium composed by two different scattering particles: organized infinite long cylinders and randomly distributed background spherical particles. The cylinders were parallel to the sample surface. A single isotropic absorption coefficient μ_a was assigned to the sample. An isotropic scattering coefficient $\mu_{s,b}$ and anisotropy g_b were assigned to the background spherical particles. The conventional Henyey–Greenstein function was used as the scattering phase function for these spherical particles. The scattering coefficient $\mu_{s,c}$ of the cylinders at an incident angle ξ can be calculated as

$$\mu_{s,c}(\xi) = 2\mathrm{r}^*\mathrm{c_A}^*Q_s(\xi), \tag{1}$$

where r is the cylinder radius, c_A is the concentration of cylinders (mm^{-2}), and $Q_s(\xi)$ is the scattering efficiency and can be calculated using the algorithm described by Yousif and Boutros [17]. The volume density of the cylinders can be calculated as $c_A \times \pi r^2$. The incident angle ξ is defined as the angle formed by the incident light and the cylinder axis. $\xi = 0°$ indicates light incident along the cylinder; whereas $\xi = 90°$ indicates light incident perpendicularly to the cylinder.

The light scattering direction by a cylinder can be defined by the following two angles: the angle between the scattered light and the cylinder axis, which is the same as the incident angle ξ, and the scattering angle ϕ, defined as the angle between the incident and scattered light within a projection plane perpendicular to the cylinder. Therefore the scattered light is restricted to a cone with the cylinder as the axis and has a half-angle of ξ [18]. Following the conventional definition, the scattering angle θ is defined as the angle between the incident and scattering directions. The corresponding scattering anisotropy g_c can be then derived as

$$g_c(\xi) = \langle \cos\theta \rangle = \cos^2\xi + \sin^2\xi \frac{\int_0^\pi \cos\phi p(\phi,\xi)\sin\phi \mathrm{d}\phi}{\int_0^\pi p(\phi,\xi)\sin\phi \mathrm{d}\phi}. \tag{2}$$

The scattering phase function $p(\phi,\xi)$ can be calculated using Yousif and Boutros's method [17]. When incident along the cylinder ($\xi = 0$), light is not scattered and thus $g_c = 1$. The reduced scattering coefficient of the cylinders is calculated as $\mu'_{s,c} = \mu_{s,c}(1 - g_c)$. The total reduce scattering coefficient of the sample is $\mu_s' = \mu_{s,c}' + \mu_{s,b}'$, which is also a function of the incident angle ξ.

B. Monte Carlo Algorithm

The simulated imaging setup is shown in Fig. 1(b). A pencil beam ($\lambda = 800\,\mathrm{nm}$) was incident at 90° upon the semi-infinite sample. The backscattered light at the sample surface was directly imaged by a CCD camera. The movement of a photon packet inside the sample was determined based on the local scattering and absorption coefficients [19]. At each scattering event, a sampling method was applied to determine whether the photon was scattered by the cylinders or the background spherical particles:

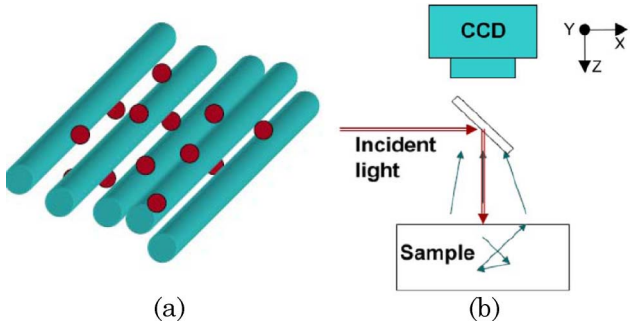

Fig. 1. (Color online) (a) Illustration of the scattering medium, which is composed of infinite long cylinders and uniformly distributed spherical particles. (b) Schematic diagram of the simulated experimental setup.

$$\text{if } \zeta < \frac{\mu_{s,c}}{\mu_{s,c}+\mu_{s,b}}, \qquad \text{scattered by cylinders,} \tag{3}$$

otherwise, scattered by spherical particles, where ζ is a uniformly distributed random number between $[0,1]$. If the photon was scattered by spherical particles, the standard procedure [19] using the Henyey–Greenstein phase function was applied to determine the scattering direction. If the photon was scattered by cylinders, the new photon direction was determined by sampling the cylindrical scattering phase function $p(\phi,\xi)$. To expedite the computation, the cylindrical scattering phase function was precalculated at different incident and scattering angles at a 0.5° precision and loaded into the Monte Carlo program at the beginning of the simulation. To determine the scattering direction, the incident direction ξ of a photon was used as an index to retrieve the stored cylinder phase function. If the phase function was not precalculated at this particular incident angle, linear interpolation was applied by using the phase functions calculated at the two closest angles to obtain the function at this particular angle. The new photon scattering angle ϕ was then sampled from the phase function $p(\phi,\xi)$:

$$\zeta \le \frac{\sum_{\phi=0}^{\phi} p(\phi,\xi)}{\sum_{\phi=0}^{180} p(\phi,\xi)}, \tag{4}$$

where ζ is a uniformly distributed random number between $[0,1]$. The simulation process continued until a photon was completely absorbed in the medium or re-emitted out of the sample. The physical location and weight of the re-emitted photon were then stored in arrays to represent 2D images of the diffuse reflectance.

C. Image Processing

The equi-intensity profiles were obtained by extracting all pixels with the same reflectance. Specifically, a pixel located at a specific distance from the incident point was selected, and its intensity was set as a reference to find all pixels with the same intensity. A $\pm 1\%$ error margin was applied in the search and the coordinates of all identified pixels were stored. Then the Levenberg–Marquardt algorithm was applied to obtain the best numerical fitting using the following parametric equation $f(x,y)$ [20]:

$$f(x,y) = \left(\frac{|x|}{r_x}\right)^q + \left(\frac{|y|}{r_y}\right)^q - 1 = 0, \tag{5}$$

where the r_x and r_y represent the half axial length along the x and y axes, respectively. In the simulation, the cylinders were always aligned with the y axis. The shape parameter q represents the geometrical shape of the equi-intensity profile with $q=1$ indicating a rhombus and $q=2$ indicating an ellipse. This parametric function can represent any geometric shape between a perfect rhombus and a perfect ellipse [20]. The ratio of the two axes was calculated as

$$\beta = r_y/r_x. \tag{6}$$

3. Results

Figure 2(a) shows an example of the reflectance image in an isotropic medium (without any embedded cylinders). The image was shown using a pseudocolor map with different colors indicating different reflectance. The following optical properties were used for this isotropic medium: $\mu_{s,b} = 30.0\,\text{cm}^{-1}$, $g_b = 0.8$, and $\mu_a = 0.01\,\text{cm}^{-1}$. The simulated reflectance image had a pixel resolution of $100\,\mu\text{m}$ and a size of $5 \times 5\,\text{cm}^2$. In order to have a better view of the reflectance distributions close to the incident point, images with a higher resolution of $10\,\mu\text{m}$ but a smaller size of $1 \times 1\,\text{cm}^2$ are also shown. The dotted lines in the images were example fitting results using Eq. (5). The equi-intensity distribution of the isotropic medium was a circle. Figure 2(c) shows the axes ratio β and the q parameter obtained by fitting the corresponding spatial resolved reflectance images in Fig. 2(a). The fitted results were axes ratio $\beta = 1.0$ and $q \sim 2.0$, indicating a perfect circular profile.

As a comparison, Fig. 2(b) shows a reflectance image obtained in an anisotropic medium where the cylindrical component had a radius of $r = 1.5\,\mu\text{m}$, a refractive index of $n_c = 1.46$, a volume density of $\rho = 0.98\%$, and a background refractive index $n = 1.36$. The corresponding scattering coefficient was $\mu_{s,c} = 109.1\,\text{cm}^{-1}$ and anisotropy $g_c = 0.945$, both at an incident angle of $\xi = 90°$. The background spherical scatters had $\mu_{s,b} = 30.0\,\text{cm}^{-1}$ and $g_b = 0.8$. The absorption coefficient was $\mu_a = 0.01\,\text{cm}^{-1}$. The cylinders were aligned with the y axis. As shown in Fig. 2(b), the equi-intensity profile of the reflectance image showed an ellipse perpendicular to the cylinder at a small distance from the incidence, whereas the ellipse became parallel to the cylinders at large distance. These observations were confirmed by the fitting results as shown in Fig. 2(d). The q parameter at near distance had a value of ~2.0, indicating an ellipse. It decreased to ~1.6 at ~0.04 cm and increased again until stabilizing at ~2.0. At the same time, the axes ratio β decreased from 0.9 to 0.8, increased thereafter and stabilized at ~1.12.

Therefore, as the evaluation distance increased, the fitting parameters β and q went through a transition and stabilized as an ellipse along the cylinders at larger distances. To better describe this transition, a "transition distance" can be defined as the distance from the incident point where the fitted axes ratio reached 90% of the final stable value.

Figure 3(a) shows the stable fitted axes ratio β obtained in anisotropic media with three different cylinder radii of 0.1, 0.25, and $1.5\,\mu\text{m}$. The β results were plotted against the ADE predictions, i.e., the square root of $\mu_s'(x)/\mu_s'(y)$, where $\mu_s'(x)$ and $\mu_s'(y)$ are the reduced scattering coefficients perpendicular and parallel to the cylinder, respectively. The dash

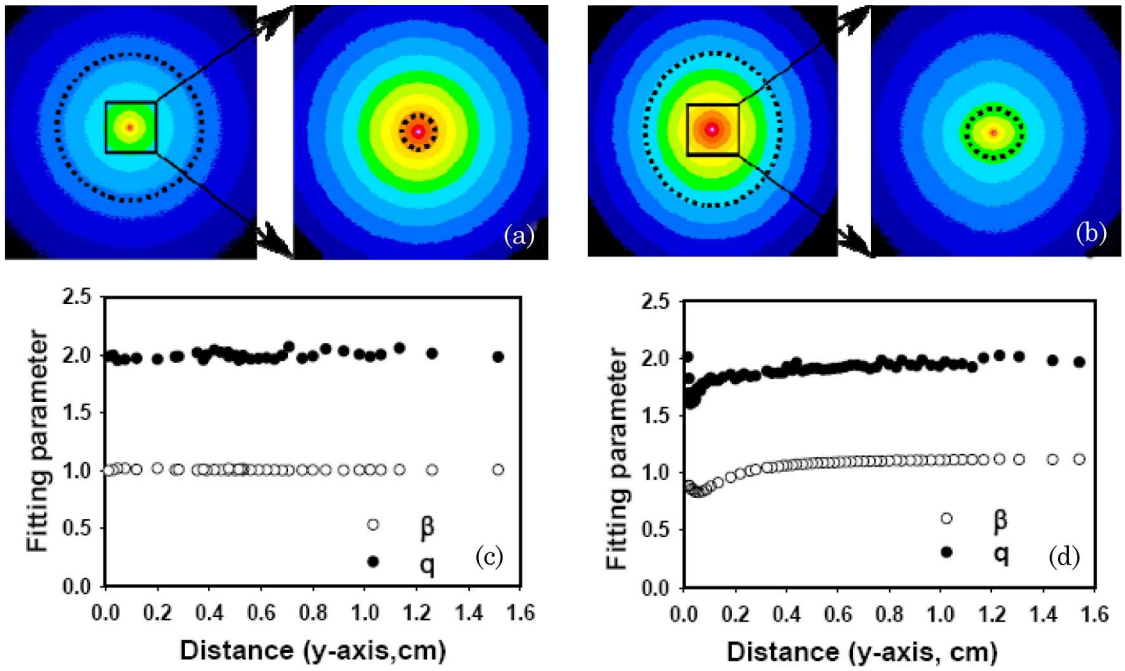

Fig. 2. (Color online) Sample reflectance images obtained in (a) isotropic and (b) anisotropic mediums. The cylinders were aligned with the y axis (vertical direction). The dash lines were sample fitting results using Eq. (5). The fitting parameters β and q were shown as a function of the distance along the y axis in the above (c) isotropic and (d) anisotropic media.

line in Fig. 3(a) shows the prediction from ADE theory that the axes ratio $\beta = r_y/r_x$ is equal to $\sqrt{\mu_s'(x)/\mu_s'(y)}$. The background optical properties were maintained at $\mu_{s,b} = 30\,\mathrm{cm}^{-1}$, $g_b = 0.8$, and $\mu_a = 0.01\,\mathrm{cm}^{-1}$. We altered $\sqrt{\mu_s'(x)/\mu_s'(y)}$ by changing the concentration of the cylinders (c_A) in the medium. The cylinder volume densities (ρ) in all samples ranged from 0.14% to 0.98%.

A linear relationship was observed between $\sqrt{\mu_s'(x)/\mu_s'(y)}$ and the fitted axes ratio β at all cylinder sizes. As shown in Fig. 3(a), all data points can be linearly fitted with $R^2 \geq 0.99$. However, the fitted lines had different slopes: 0.95, 0.82, and 0.29 for cylinders with radius of 0.1, 0.25, and 1.5 μm, respectively. The point $(1,1)$ represents the results from isotropic samples. All regression lines in Fig. 3(a) passed through the point $(1,1)$ with a very small standard error of intercept (<0.015%). Interestingly, when the cylinder radius was small (0.1 μm), the fitted axes ratio β from the Monte Carlo simulations approached the prediction from the ADE theory. To further confirm this, the fitted axes ratio β was calculated at different cylinder radii from 0.05 to 1.5 μm, while $\sqrt{\mu_s'(x)/\mu_s'(y)}$ was maintained at a constant value of 1.08. The background optical properties were the same as before. The cylinder volume densities (ρ)

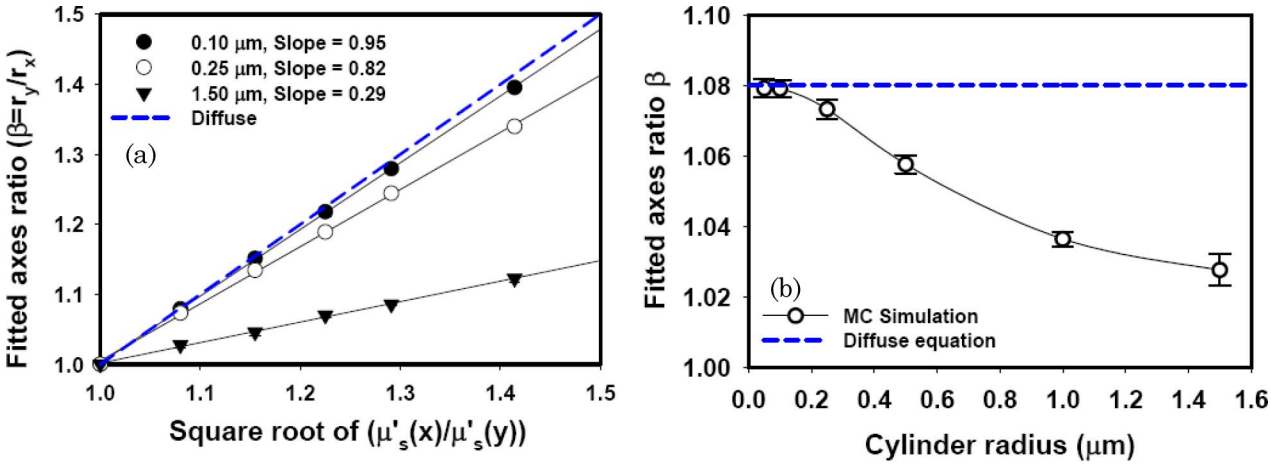

Fig. 3. (Color online) (a) Fitted axes ratio β versus the ADE prediction of $\sqrt{\mu_s'(x)/\mu_s'(y)}$ in anisotropic media of three different cylinder radii: 0.1, 0.25, and 1.5 μm. The background optical properties used in the simulation were $\mu_{s,b} = 30\,\mathrm{cm}^{-1}$, $g_b = 0.8$, and $\mu_a = 0.01\,\mathrm{cm}^{-1}$. (b) Fitted axes ratio β versus cylinder radius. $\sqrt{\mu_s'(x)/\mu_s'(y)}$ was maintained at constant value of 1.08.

in all samples ranged from 0.14% to 0.30%. As shown below in Fig. 5(b), β indeed approached the ADE prediction when the cylinder radius was small.

A small variation in cylinder refractive index n_c had little effect on the fitted axes ratio β. Using cylinders with a radius of $r = 0.1\,\mu$m, the calculated β had less than 0.5% variation when the cylinder refractive index was changed from 1.44 to 1.48. In the above calculation, the background optical properties were maintained at $\mu_{s,b} = 30\,\text{cm}^{-1}$, $g_b = 0.8$, and $\mu_a = 0.01\,\text{cm}^{-1}$, and the $\sqrt{\mu_s'(x)/\mu_s'(y)}$ was maintained at a constant value of 1.29.

Figure 4 shows the effects of background optical properties on the geometric profiles of the simulated diffuse reflectance. We also calculated the transition distance as defined above and the total diffuse reflectance. Unless otherwise indicated, the optical properties used in the simulation were the cylinder radius $r = 0.1\,\mu$m, $n_c = 1.46$, $\mu_{s,b} = 30\,\text{cm}^{-1}$, $g_b = 0.8$, and $\mu_a = 0.01\,\text{cm}^{-1}$. $\sqrt{\mu_s'(x)/\mu_s'(y)}$ was maintained at a constant value of 1.08.

Figure 4(a) shows the fitted axes ratio β and total diffuse reflectance at different background scattering coefficients from $\mu_{s,b} = 15$ to $60\,\text{cm}^{-1}$. In order to

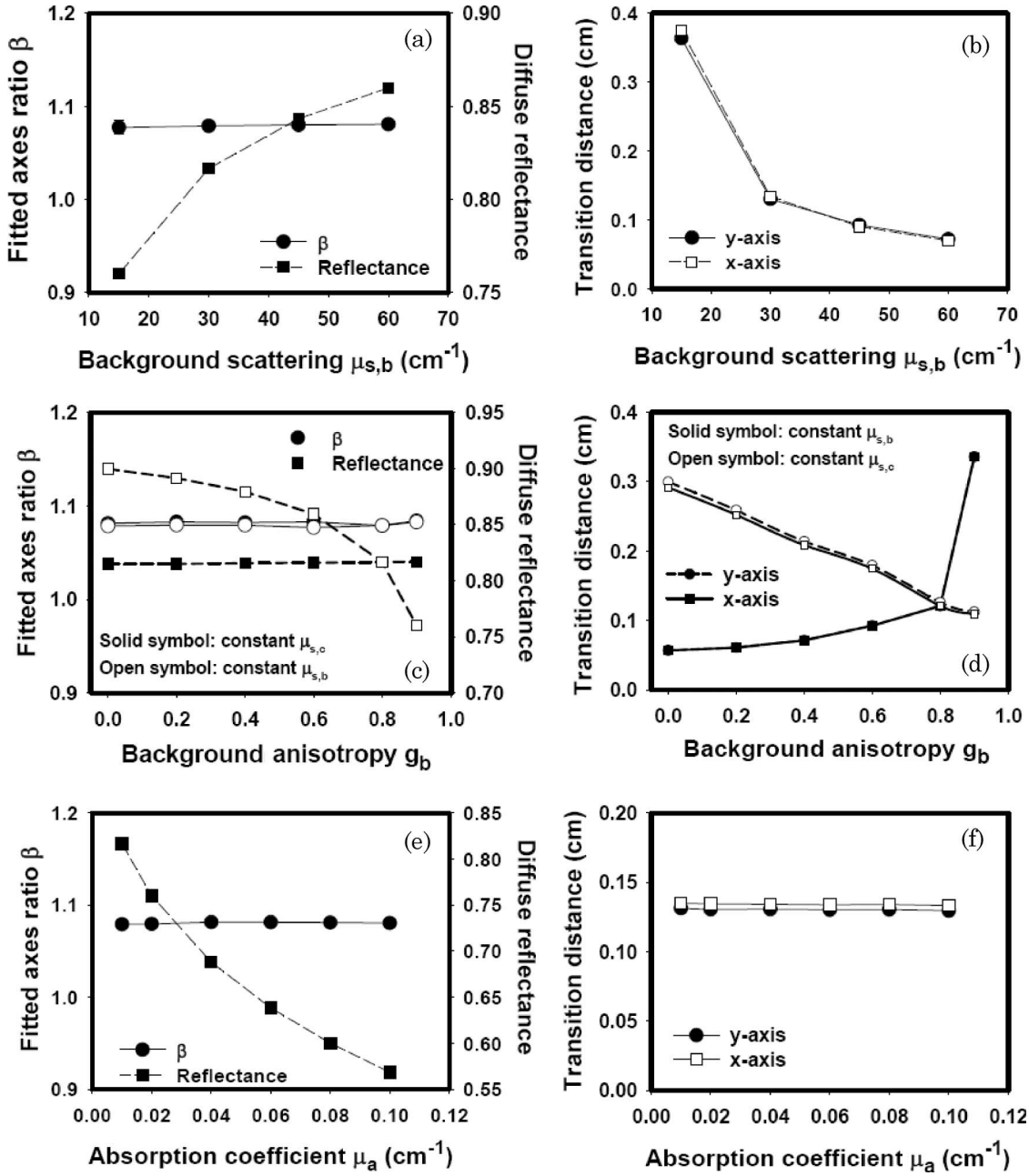

Fig. 4. (Color online) Fitted axes ratio β and total diffuse reflectance at different (a) background scattering coefficients $\mu_{s,b}$, (c) background anisotropies g_b, and (e) absorption coefficients μ_a. The corresponding transition distances were shown in (b), (d), and (f), respectively. Unless otherwise indicated, the optical properties in the simulation were $r = 0.1\,\mu$m, $\mu_{s,b} = 30\,\text{cm}^{-1}$, $g_b = 0.8$, $\mu_a = 0.01\,\text{cm}^{-1}$, and $\sqrt{\mu_s'(x)/\mu_s'(y)} = 1.08$.

maintain $\sqrt{\mu_s'(x)/\mu_s'(y)}$, the cylinder volume densities were varied from $\rho = 0.07\%$ to 0.27%, respectively. The result indicated that the background scattering coefficient had no significant effect on the fitted axes ratio when $\sqrt{\mu_s'(x)/\mu_s'(y)}$ was the same. As expected, the total diffuse reflectance increased with the background scattering coefficient. However, the transition distance decreased as the background scattering coefficient increased as shown in Fig. 4(b). The transitional distances calculated along the cylinder were nearly identical to those calculated perpendicular to cylinders.

Figure 4(c) shows the fitted axes ratio β and total diffuse reflectance at different background anisotropy values. When increasing the background g_b from 0.0 to 0.9, the $\sqrt{\mu_s'(x)/\mu_s'(y)}$ was maintained as a constant of 1.08 by either (1) maintaining background scattering $\mu_{s,b}$ and reducing cylinder volume density ρ from 0.69% to 0.07% or (2) maintaining cylinder volume density ρ and increasing background scattering coefficient $\mu_{s,b}$ from 6.0 to 60.0 cm^{-1}. In either case, the background anisotropy g_b had no effect on the fitted axes ratio β. The total diffuse reflectance decreased as the background anisotropy increased when reducing cylinder volume concentration (and thus the cylinder scattering coefficient $\mu_{s,c}$). But it did not change with g_b when increasing $\mu_{s,b}$ but maintaining the $\mu_{s,b}'$. On the other hand, the transition distance decreased with the background anisotropy when increasing the $\mu_{s,b}$, whereas the transition distance increased with the background anisotropy when reducing $\mu_{s,c}$, as shown in Fig. 4(d).

Figure 4(e) shows the fitted axes ratio β and total diffuse reflectance at different background absorption coefficients from $\mu_a = 0.01$ to 0.1 cm^{-1}. The cylinder volume density was kept at $\rho = 0.14\%$. The result indicated that the total diffuse reflectance decreased as the absorption coefficient increased. However, the background absorption coefficient had no significant effect on the axes ratio and the transition distance as shown in Fig. 4(f).

4. Discussion

As predicted from the ADE and CTRW theories, Monte Carlo simulation showed the equi-intensity reflectance in a fibrous turbid medium had an elliptic shape. The elliptical patterns were inclined to the fiber axis where the total reduced scattering coefficient μ_s' is the smallest of those at any other directions. The ADE also predicts that the ratio of the two orthogonal axial lengths in the elliptical distribution is inversely proportional to the square root of corresponding reduced scattering coefficients perpendicular and parallel to the fibrous structures [6,8]: $r_y/r_x = \sqrt{\mu_s'(x)/\mu_s'(y)}$. However, the Monte Carlo simulation indicated that this is true only for small cylinders. At a constant $\sqrt{\mu_s'(x)/\mu_s'(y)}$, the elliptical equi-intensity patterns were much less elongated for cylinders of 1.5 μm radius than those of 0.1 μm radius.

The observed size dependency is likely due to the different scattering efficiency and anisotropy profiles at different cylinder sizes. Figure 5 shows the scattering efficiency and anisotropy calculated for cylinders of different radii. Both the scattering efficiency and anisotropy depended on the incident direction of the photon relative to the cylinder axis. The anisotropy of small cylinders acted more like an isotropic than an anisotropic scatterer at large incident angles of $\xi > 45°$ because of the small anisotropy. On the contrary, for cylinders of a large radius, the anisotropy was ~0.9 at large incident angles, indicating a predominantly forward scattering. Therefore, photons that were incident at large angles had much less chance to be scattered back toward the large cylinders than small cylinders. In addition, when $\xi > 30°$, the scattering efficiency value for large cylinders was significantly larger than small cylinders. So photons experienced more scattering by large cylinders at large incident angles. Overall, photons propagated farther along the cylinders than across the cylinders, but such inclination was greater for small cylinders. The fitted axes ratio β in anisotropic media of small cylinders was closer to the ADE prediction, which appeared to be an extreme limit for small cylinders.

We found that when $\sqrt{\mu_s'(x)/\mu_s'(y)}$ was maintained at a constant value, the fitted axes ratio β was not affected by varying the background optical properties when evaluated far away from the incident point. In other words, the geometric shape of the diffuse reflectance was only determined by the ratio of the

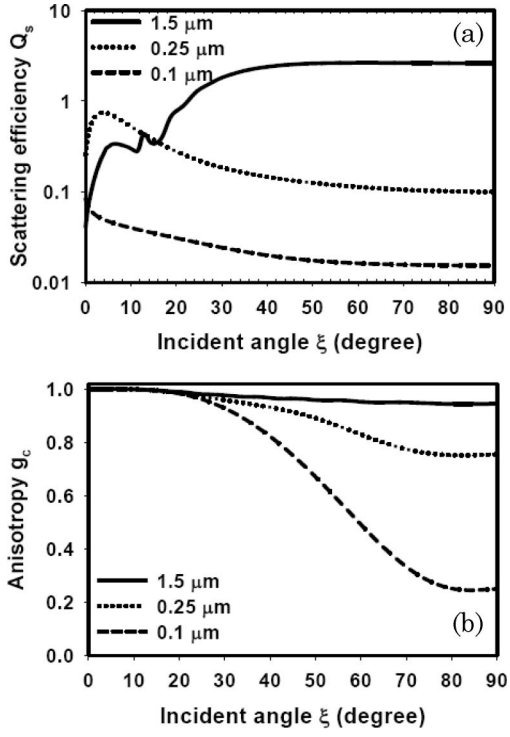

Fig. 5. (Color online) (a) Scattering efficiency Q_s and (b) anisotropy g_c as a function of incident angle ξ for cylinders of different radii.

total reduced scattering coefficient along the two primary axes. However, the total diffuse reflectance was affected by all of the background optical properties. In agreement with diffuse theory, the total diffuse reflectance generally decreased as the absorption coefficient increased, and increased as reduced scattering coefficient increased.

The transition distance was also affected by the scattering coefficient. It is known that single scattering is important at locations closer to the incident point, while multiple scattering becomes dominant at larger distances. At a certain distance from the incident, a photon undergoes a higher number of scattering events in samples with higher scattering coefficients. In other words, a higher background scattering coefficient reduces the transport distance required for the transition from single scattering to multiple scattering, which results in a smaller transition distance as shown in Fig. 4(b). The effects of background anisotropy in Fig. 4(d) can also be explained in the same way due to the changes in either the background scattering coefficient or the cylinder scattering coefficient. Because the overall absorption coefficients were much smaller than the scattering coefficients, changes in absorption coefficient had little effect on the transition distance.

5. Conclusion

In summary, Monte Carlo simulation was employed to simulate the propagation of light in a fibrous anisotropic scattering medium. The spatial profiles of the diffuse reflectance were quantitatively analyzed using a numerical fitting algorithm. The results indicated that the equi-intensity profiles of the surface reflectance always had elliptic distributions when evaluated at larger distances from the incidence. The shape of the elliptical distribution was not affected by the background optical properties when the ratio of the total reduced scattering coefficients parallel and perpendicular to the cylinder was maintained constant. The prediction of the anisotropic diffuse equation theory was in agreement with the Monte Carlo simulation only for small cylinders. As fiber diameters in biological tissue may vary from tens of nanometers to hundreds of microns, caution should be taken when applying diffuse theory to study light propagation in fibrous tissues.

This project was supported in part by National Science Foundation (NSF) grant CBET0643190.

References

1. G. Marquez, L. V. Wang, S.-P. Lin, J. A. Schwartz, and S. L. Thomsen, "Anisotropy in the absorption and scattering spectra of chicken breast tissue," Appl. Opt. **37**, 798–804 (1998).
2. S. Nickell, M. Hermann, M. Essenpreis, T. J. Farrell, U. Krämer, and M. S. Patterson, "Anisotropy of light propagation in human skin," Phys. Med. Biol. **45**, 2873 (2000).
3. F. K. Forster, A. Kienle, and R. Hibst, "Determination of the optical parameters of dentin from spatially resolved reflectance and transmittance measurements," Proc. SPIE **4432**, 103–109 (2001).
4. M. Moseley, Y. Cohen, J. Kucharczyk, J. Mintorovitch, H. Asgari, M. Wendland, J. Tsuruda, and D. Norman, "Diffusion-weighted MR imaging of anisotropic water diffusion in cat central nervous system," Radiology (Oak Brook, Ill.) **176**, 439–445 (1990).
5. H. Stark and T. C. Lubensky, "Multiple light scattering in nematic liquid crystals," Phys. Rev. Lett. **77**, 2229 (1996).
6. J. Heino, S. Arridge, J. Sikora, and E. Somersalo, "Anisotropic effects in highly scattering media," Phys. Rev. E **68**, 031908 (2003).
7. P. M. Johnson, B. P. J. Bret, J. G. Rivas, J. J. Kelly, and A. Lagendijk, "Anisotropic diffusion of light in a strongly scattering material," Phys. Rev. Lett. **89**, 243901 (2002).
8. L. Dagdug, G. H. Weiss, and A. H. Gandjbakhche, "Effects of anisotropic optical properties on photon migration in structured tissues," Phys. Med. Biol. **48**, 1361 (2003).
9. J. C. Hebden, J. J. G. Guerrero, V. Chernomordik, and A. H. Gandjbakhche, "Experimental evaluation of an anisotropic scattering model of a slab geometry," Opt. Lett. **29**, 2518–2520 (2004).
10. A. Sviridov, V. Chernomordik, M. Hassan, A. Russo, A. Eidsath, P. Smith, and A. H. Gandjbakhche, "Intensity profiles of linearly polarized light backscattered from skin and tissue-like phantoms," J. Biomed. Opt. **10**, 014012–014019 (2005).
11. J. Ranasinghesagara, F. Hsieh, and G. Yao, "A photon migration method for characterizing fiber formation in meat analogs," J. Food Sci. **71**, E227–E231 (2006).
12. A. Kienle, F. K. Forster, and R. Hibst, "Anisotropy of light propagation in biological tissue," Opt. Lett. **29**, 2617–2619 (2004).
13. A. Kienle, "Anisotropic light diffusion: an oxymoron?," Phys. Rev. Lett. **98**, 218104 (2007).
14. J. Schafer and A. Kienle, "Scattering of light by multiple dielectric cylinders: comparison of radiative transfer and Maxwell theory," Opt. Lett. **33**, 2413–2415 (2008).
15. A. Kienle, F. K. Forster, R. Diebolder, and R. Hibst, "Light propagation in dentin: influence of microstructure on anisotropy," Phys. Med. Biol. **48**, N7–N14 (2003).
16. A. Kienle, C. D'Andrea, F. Foschum, P. Taroni, and A. Pifferi, "Light propagation in dry and wet softwood," Opt. Express **16**, 9895–9906 (2008).
17. H. A. Yousif and E. Boutros, "A FORTRAN code for the scattering of EM plane waves by an infinitely long cylinder at oblique incidence," Comp. Phys. Commun. **69**, 406–414 (1992).
18. C. F. Bohern and D. R. Huffman, *Absorption and Scattering of Light by Small Particles* (Wiley, 1983).
19. L. V. Wang, S. L. Jacques, and L. Zheng, "MCML—Monte Carlo modeling of light transport in multi-layered tissues," Comput. Methods Programs Biomed. **47**, 131–146 (1995).
20. J. Ranasinghesagara and G. Yao, "Imaging 2D optical diffuse reflectance in skeletal muscle," Opt. Express **15**, 3998–4007 (2007).